International Journal of Engineering and Advanced Technology (IJEAT)
ISSN: 2249-8958 (Online), Volume-13 Issue-6, August 2024

Impact Mechanics of Thin Metal Plates Using Lagrangian, CEL and SPH Methods

M. Marri, R. Ahmed

Abstract: ***This paper aimed to evaluate the ballistic limit for high-speed perpendicular and oblique impacts on thin aluminium alloy (AA6061-T651, Al5052) plates. Finite Element Analysis (FEA) was conducted on a commercially available software, Abaqus/Explicit®. The impact velocities in the model ranged from 100 m/s to 1000 m/s. Three distinctive modelling techniques were compared for simulating high-speed impacts, i.e., Smoothed Particle Hydrodynamics (SPH), Coupled Eulerian and Lagrangian (CEL) and Lagrangian. This investigation considered two different projectile shapes, i.e., conical and blunt. Plate thickness varied as 16, 20, and 26.3mm using the Lagrangian analysis. The influence of the physical properties of projectiles was analysed by comparing deformable and analytically rigid projectiles. The results of this study showed a good agreement with published data (experimental and FEA) for the Lagrangian model for both perpendicular and oblique impacts. The CEL method overestimated the ballistic limit, whereas the SPH model slightly underestimated the ballistic limit. The accuracy of the SPH model was velocity dependent, with a % error ranging from 3% (higher velocity) to 21% (lower velocity). The CEL model also showed velocity-dependent accuracy. The CEL model showed the highest percentage of energy absorption during contact interaction at the ballistic limit for perpendicular conical impacts. In contrast, Lagrangian and SPH models showed very similar energy absorption results for the blunt projectiles regardless of the impact angle. Changing the deformable projectile to analytical rigid varied the velocity-dependent % error from 2 to 38%.***

Keywords: ABAQUS, Coupled Eulerian-Lagrangian (CEL), Finite element modelling, High-Speed Interactions, Impact Mechanics, Smoothed Particle Hydrodynamics (SPH).

Abbreviation

CEL	Coupled Eulerian and Lagrangian
C3D8R	Continuum 3D 8 nodes reduced integration
DEM	Discrete Element Method
EoS	Equation of State
EFG	Element-Free Galerkin Method
EC3D8R	Eulerian Continuum 3D 8 nodes reduced integration
EVF	Eulerian Volume Fraction
Eb	Projectile energy at the ballistic limit, J
Ei	Initial projectile energy, J
FEM	Finite Element Method
GFEM	Generalized Finite Element Method
MPM	Material Point Method
PFEM	Particle Finite Element Method
PC3D	Continuum particle 3D elements
SPH	Smoothed Particle Hydrodynamics
Vb	Ballistic Velocity, m/s
Vi	Initial Velocity, m/s

Nomenclature

ρ	Density, kg/m^3
$\dot{\varepsilon}^*$	Dimensionless plastic strain
σ_{eq}	Equivalent stress
A	JC static yield stress, Pa
B	JC strain hardening modulus, Pa
JC	Johnson Cook
W	Kernel function
σ_m	Mean stress, Pa
$\theta_{melting}$	Melting Temperature, K
Γ0	Mie-Gruneisen constant
μs	micro-seconds
D1 to D5	Model constants
ρ_j	Particle density
m_j	Particle mass
j	Particles
ε	Plastic strain
$\dot{\varepsilon_p}^*$	Plastic strain rate or effective strain rate
$\dot{\varepsilon}$	Reference strain rate
T_{Ref}	Reference Temperature, K
f_j	Sampled through the sampling function (Kernel)
s	Shock velocity
h	Smoothing length
c_v	Specific heat, J/kgK
C_0	Speed of sound, m/s
n	Strain hardening coefficient
c	Strengthening strain rate
m	Thermal softening coefficient
T^*	Transition temperature, K

I. INTRODUCTION

Supersonic impact mechanics is an extensively researched area due to its utility in civil and military applications [1]. These investigations range from the hard perforation of projectiles, the soft impact of bird strikes on aircraft structures, and the hypersonic impacts of debri interaction with space vehicles [2-6]. Bird strikes, as a significant soft-body effect, have become an exceedingly dangerous and tragic problem in the civil aviation industry, risking the safety of passengers and aircraft [3].

Manuscript received on 20 June 2024 | Revised Manuscript received on 27 July 2024 | Manuscript Accepted on 15 August 2024 | Manuscript published on 30 August 2024.

***Correspondence Author(s)**
Mahendher Marri*, School of Engineering and Physical Sciences, Heriot-Watt University, Edinburgh EH14 4AS, UK. E-mail ID: mahendher.marri1@gmail.com, ORCID ID: 0000-0002-4532-3722
Dr. Rehan Ahmed, School of Engineering and Physical Sciences, Heriot-Watt University, Edinburgh EH14 4AS, UK E-mail ID: r.ahmed@hw.ac.uk

Retrieval Number: 100.1/ijeat.F452813060824
DOI: 10.35940/ijeat.F4528.13060824
Journal Website: www.ijeat.org

Published By:
Blue Eyes Intelligence Engineering and Sciences Publication (BEIESP)

Similarly, protecting personnel using body armour whilst operating in dangerous environments, such as clearing landmines, can be improved by better understanding hard projectile impacts [1]. Understanding high-speed impact mechanics has helped analyse iterations in spacecraft structures [4] and advanced manufacturing techniques utilising high-speed impacts [7].

Both numerical and experimental approaches have been adapted in the published literature to investigate the perforation of hard projectiles on various engineering materials. Table 1 [1-3, 7-32] summarises the analysis of the literature on various high-speed impacts on metal alloys and composites using different simulation techniques. This analysis showed a significant difference between the modelling techniques: Lagrangian, SPH, and CEL, based on model accuracy, impact angle and velocity. In some cases, Lagrangian showed the highest accuracy (~98%) between experimental data and analytical equations [1, 14]. These investigations indicate that impact and perforation behaviour depends on the material, velocity, impact angle, projectile shape, and the modelling technique. There is limited literature on investigations comparing the influence of modelling methodology on the impact behaviour of high-speed projectiles [1]. This investigation aimed to compare this dependency of the modelling approach using Lagrangian, Coupled Eulerian and Lagrangian (CEL) and Smoothed Particle Hydrodynamics (SPH) methods on the perforation of conical and blunt projectiles for a range of velocities and angle of impact. Results are validated using published literature and analysed to compare the influence of the modelling technique. Ballistic limits, defined as the minimal velocity required to perforate the target, are compared to the modelling techniques, projectile nose shape, and impact angle.

II. FINITE ELEMENT MODEL DESCRIPTION

Lagrangian, CEL and SPH models were simulated in Abaqus/Explicit®. Table 2 summarises the parameters of velocities, impact angle, material, and projectile shape analysed in this study. Dimensions of the projectile (Conical and Blunt) and target (26.3mm thickness) are summarised in Figure 1a and 1b, respectively. Projectile velocity varied between 100 to 1000 m/s with an increment of 100m/s.

Table 1. Summarise Literature Survey of Various Models and Experiments for Impact

Material	Type of step	Validation	Description	Solver	Ref
Ti6Al-4V	Lagrangian	FEA results are compared with experiments. Showed ~96% accuracy to experiment results.	Ti6Al-4V and carbon steel substrate are used as target materials. Placing Ti6Al-4V as a bilayer on carbon steel can withstand the impact due to ballistic impact.	ABAQUS/Explicit	[1]
Al 2024-T3	Analytical equations	Analytical results compared with published experimental data. Accuracy is ~97%.	Three materials are studied using analytical equations with cone and ovoid projectiles. Impact angles are 0, 30 and 45.	Analytical equations	[2]
CFRP	SPH-FEM	FEA results are compared with experiments. FEA accuracy is ~75-80%.	The composite plate is used as a target with 0,45,0-45s ply angles.	ABAQUS/Explicit	[3]
Yttrium-stabilised zirconia (YSZ)	Coupled Eulerian and Lagrangian (CEL)	FEA results compared with published data. The accuracy is ~85%.	High-speed spray coating was simulated using the CEL method.	ABAQUS/Explicit	[7]
Steel 4340	Lagrangian	FEA results are validated with experimental data. The accuracy is ~90%.	Target perforated at 396 m/s. Ogive nose projectile demonstrated excellent quantitative and qualitative agreement with experimental outcomes.	ABAQUS/Explicit	[8]
Al2017	Material Point Method (MPM)	Parametric study by varying impact velocity and face sheet size. The accuracy is ~75%.	High-velocity perforation of honeycomb was studied for 4 and 5km/s. Placing an intermediate face sheet between honeycomb is not the best choice. However, making this face sheet into multiple thicknesses can improve the resistance.	MPM and SPH	[9]
Al6061-T651	Lagrangian	Simulated results are compared with experimental data. The simulation showed 96.4% accuracy between simulation and experimental data.	Three different configurations (impact angles) with two projectiles are used. Striking velocities are varied from 1000-7000m/s.	ABAQUS/Explicit	[10]
Al2024	Combined Lagrangian and SPH	Parametric study on egg box shield to test impact size, cell size, and axial offset. The accuracy is ~65-80%.	The egg box shield was designed and simulated based on a flat panel. The outcomes showed that energy absorption is high, with a decrease in derbies.	LS-DYNA	[11]
Al2024	SPH (MPM)	Validated the simulation results with fitting curves. ~95% accuracy was	Normal and oblique impacts are simulated. Normal impacts are influenced by high energy flux.	LEO environment	[12]

Retrieval Number: 100.1/ijeat.F452813060824
DOI: 10.35940/ijeat.F4528.13060824
Journal Website: www.ijeat.org

Published By:
Blue Eyes Intelligence Engineering and Sciences Publication (BEIESP)

		achieved between fitting curves and simulation.			
AA2024-T3	SPH	FEA is compared with experimental results. FEA presented ~95% accuracy to the experiment.	Three different projectiles (hemispherical, conical, and blunt) are used for simulation with a velocity range from 50-200m/s. Nose shape can influence the kinetic energy into local energy.	ABAQUS/Explicit	[13]
AISI 4340-H steel alloy	Lagrangian	FEA is compared with experimental results. FEA presented ~92% accuracy when compared to the experiment.	Initial velocities from 930 m/s to 1400 m/s for both experimental and simulation.	LS-DYNA	[14]
7.62AP	Lagrangian	FEA results are validated with experimental data. The accuracy is ~99%.	The target was perforated with a conical projectile at 133 m/s.	ABAQUS/Explicit	[15]
Steel 4340	Experiment	Perforation of projectiles is validated with mathematical equations with an accuracy of ~94%.	Target perforated at 308 m/s. Ogive nose projectile perforated at 341 m/s. A qualitative agreement was achieved between the experiment and derived equations.	Experiment	[16]
CFRP T300/914	Coupled Eulerian and Lagrangian (CEL)	FEA results compared with published data. Approx. 80% accurate to published data.	A bird strike (150m/s) simulation was carried out on composite to find the accuracy of Lagrangian and CEL modelling techniques. CEL showed an improvement in accuracy in finding fluid behaviour as compared to Lagrangian.	ABAQUS/Explicit	[17]
AISI-1045 steel	Experiment and fmincon	FEA and nonlinear programming results are compared with the experiment. The results obtained showed good agreement with the experimental method. The accuracy is ~70-85%.	Optimisation of medium carbon steel was performed with the help of tensile, FEA, and nonlinear programming.	Experiment and fmincon	[18]
Armor steel	Lagrangian	Simulated results are compared with experiments. The accuracy is ~80%.	Johnson and cook damage parameters are evaluated for armour steel using FEA. Later, FEA results are compared with the Charpy impact test. FEA results were in close agreement with experimental data.	Experiment and ABAQUS	[19]
CF/Epoxy	Lagrangian	FEA results are compared with published data. The accuracy is ~85-94%.	This work predicted impact damages in computational methods. It predicted delamination damage for low velocity and perforation for high-impact energies.	PAM-CRASH	[20]
Epoxy and Spectra	Lagrangian	FEA results are compared with published data. The accuracy is ~87-92%.	Gradient design composite armours were simulated in ABAQUS and ALGOR packages. Fibre/Epoxy showed good resistance during oblique impact.	ABAQUS and ALGOR	[21]
AA 6082-T6	Lagrangian	FEA results are compared with experiments. The accuracy of flow stress for FEA with the experiment is ~98%, and stress triaxiality is higher at the cross-section.	Flow and fracture analysis of AA6082-T6 at different strain rates and triaxialities.	ABAQUS/Explicit	[22]
Metglas 2605 SA1	Experiment	A hypervelocity (7000m/s) impact experiment is carried out on a Whipple shield integrated with metallic glass. The accuracy is ~75-83%.	The experiment concludes that using metallic glass can prevent perforation compared to fabric layers.	Experiment	[23]
carbon (T800), E-glass, and PA	Experiment and Lagrangian	FEA results compared with experimental data. The accuracy is ~62.2%.	Calibration of carbon, E-Glass, and PA material composites using tensile test.	LS-DYNA	[24]
OFHC copper, Armco iron and 4340 steel	Experiment	The mechanical properties of the material are derived. The accuracy between materials is ~75%.	A fracture characteristics test was carried out on a material list under torsional over various strain rates. The Hopkinson bar test was employed to conduct the experiment.	Experiment	[25]
-	SPH	FEA approximation is compared with published data. The accuracy is ~86%.	SPH approximation is carried out using partial differential equations.	Experiment/FEA	[26]
AA 5754-H111, AA 6082-T6	Experiment	The accuracy of FEA is ~94% compared to published data.	A high-speed perforation test was done on aluminium alloys using three projectiles: conical, hemispherical, and blunt. Conical	Experiment	[27]

			and blunt are very effective perforators; however, the hemispherical trend was the opposite.		
-	Both SPH and Lagrangian	FEA results are compared with the NASA ballistic curve. The accuracy is ~78-82%.	A FEA comparison of AUTODYN 2D and PAM-SHOCK 3D hydrocodes was conducted on the Whipple shield. AUTODYN 2D matched with NASA data well, and PAM-SHOCK 3D overestimated the results.	AUTODYN 2D and PAM-SHOCK 3D	[28]
Metals	Analytical equations	The thermal behaviour of Al, Cu, W and Fe was approximated. The accuracy is ~70% between materials in thermal conductivity.	In this, a thermal analysis of metal during impact was studied.	Analytical equations	[29]
AA6082-T4	Lagrangian	FEA results are compared with experiments. The accuracy of FEA is ~90% when compared with the experiment.	AA6082-T4 plate thickness of 20mm is used for normal and oblique impact tests and simulation. Two different bullets were used: hard steel core and soft core. FEA results showed good agreement with the experiment.	LS-DYNA	[30]
Kevlar/KM2, UHMWPE/Spectra1000	Experiment	Modification ISS Whipple shied was studied. The accuracy is ~95%.	A hypervelocity (3150-3350m/s) impact test was performed by replacing the conventional Kevlar with a UHMWPE shield. UHMWPE absorbed most of the energy compared to Kevlar.	Experiment	[31]
Aluminum	Empirical equations	The obtained R2 values for the different regression equations range from approximately 60% to well over 90%, which is a good range.	These formulas are derived from data found in 13 previously released papers and reports.	Empirical equations	[32]

Table 2. Projectile and Target Numerical Setup Specifications for the Current Simulation Study

Modelling Technique	Projectile Shape	Rigid/ Deformable Projectile	Velocity Range (m/s)	Projectile Material	Impact Angle	Target Material	CPU Time* (min)
Lagrangian	Conical Blunt	Deformable	100-1000	Steel 4340	Perpendicular (0º), Oblique (30º)	AA6061-T651, Al5052	90
CEL					Perpendicular (0º), Oblique (30º)	AA6061-T651, Al5052	120
SPH					Perpendicular (0º), Oblique (30º)	AA6061-T651, Al5052	200
Lagrangian	Conical Blunt Hemispherical	Rigid	100-1000	-	Perpendicular (0º)	Al6061-T651	40
CEL				-	Perpendicular (0º)	Al6061-T651	90
SPH				-	Perpendicular (0º)	Al6061-T651	130

*Note: CPU time accumulated for perpendicular and oblique impacts. It is based on Abaqus monitor status.

Table 3. List of Johnson Cook Plasticity Parameters for Projectile Material from Literature

Material	Dimensions	Velocity, m/s	A (Mpa)	B (Mpa)	n	m	$\theta_{melting}, K$	$\theta_{transition}, K$	c	$\dot{\varepsilon}$	Ref
Yttrium-stabilised zirconia (YSZ)	Particle diameter is 30micrometer	100-240	420	521	0.184	0.0197	2988	298	0.07	0.418	[7]
Steel 4340	88.9mm x 12.9mm, Nose radius 38.7mm	400-900	792	510	0.26	1	1793	293.2	0.014	1	[8]
Al2017	Ø2mm	4000-5000	265	426	0.34	1	775	293	0.015	-	[9]
Al6061-T651	Ø10mm	2000-10000	324	114	0.42	1.3	925	293.2	0.002	1	[10]
Al2024	Ø7.9mm	5600	265	426	0.34	1	775	293	0.015	-	[11]
Al2024	Ø20micrometer	700-5000	265	426	0.34	1	775	-	0.015	-	[12]
AA2024-T3	Blunt Ø13mm×29mm, Hemispherical Ø13mm×31.5,	50-200	352	440	0.42	1.7	775	293	0.008	0.0003	[13]

	Conical Ø13mm×33.95mm, θ=36 deg										
AISI 4340-H steel alloy	Ø20mm×24mm, Fillet of 350,9.5mm width	900-1500	791	510	0.26	1	1793	-	0.014	0.001	[14]
7.62AP	Ø6.06mm, nose=7.65, length=20.75mm, and total=28.4mm	445-850	2700	211	0.07	1.2	1800	293	0.005	0.0001	[15]
Al6061	Ø2mm	1300-4500	265	426	0.34	1	775	293	0.015	-	[33]
Aluminum (Al)	Ø7mm	2000-10000	337	343	0.41	1	877	293	0.01	-	[34]

Table 4. List of Johnson Cooks Plasticity Parameters for Target Material from Literature

Material	Dimensions	A (Mpa)	B (Mpa)	n	m	$\theta_{melting}$, K	$\theta_{transition}$, K	c	$\dot{\varepsilon}$	Time	Solver	Ref
Stainless steel (SS)	circular disc Dia is 100 micrometres and has a height of 37.5 micrometres	310	1000	0.65	1	1673	298	0.07	0.418	100microseconds, (ms)	ABAQUS	[7]
Al6061-T651	304mm2, 26.3mm	324.1	113.8	0.42	1.3	925	293.2	0.002	1	95ms	ABAQUS (Lagrangian)	[8]
Al2024-T81, Al5052	4.76mm x 178mm, 0.4 thick	265	426	0.34	1	775	293	0.015	-	50ms	MPM and SPH	[9]
Al6061-T6	Ø100mm, 4mm thick	324.1	113.8	0.42	1.3	925	293.2	0.002	1	25ms	ABAQUS	[10]
Al2024	The thickness of the front bumper=1mm and rear bumper=4.8mm	265	426	0.34	1	775	293	0.015	-	60ms	LS-DYNA (SPH)	[11]
Al20204	---	265	426	0.34	1	775	-	0.015	-	0.5ms	LEO environment (MPM)	[12]
AA2024-T351	130mm×130mm, Thickness=4mm	352	440	0.42	1.7	775	293	0.0083	0.00 03	0.1ms	ABAQUS (SPH)	[13]
AA7020-T651	Ø=119mm	295	260	1.65	1.3	880	-	0.000 89	0.00 01	780ms	LS-DYNA	[14]
Mild Steel	200mm x 200mm, 12 and 16mm thick plate	304.3	422.01	0.35	0.9	1800	293	0.0156	0.00 01	-	ABAQUS	[15]
Armor steel	-	980	2000	0.83	1.4	-	-	0.0026	-	-	ABAQUS	[18]
AISI-1045 steel	25mm in length and 3mm in thickness	50.103	176.091	0.5176	0.6622	1223	298	0.095	0.001	-	Experimental and fmincon	[19]
AA6082-T6	-	277.33	307.93	0.69	1.28	-	-	0.0032	0.00 01	-	ABAQUS	[22]
Al5052	D=3mm, thickness=0.5 mm, height=14.2mm	265	426	0.34	1	775	293	0.015	-	30ms	LS-DYNA	[33]
Aluminum (Al)	20mm, 0.8mm thick	337	343	0.41	1	877	293	0.01	-	10ms	Ouranos hydrodynamic	[34]

Table 5. Equation of State and Johnson Cook Failure Parameters from the Literature

Material	$\rho, \frac{kg}{m^3}$	Γ_0	$C_0, \frac{m}{s}$	s	T_{Ref}, K	$c_v, \frac{J}{kgK}$	D_1	D_2	D_3	D_4	D_5	Ref
Projectiles												
Ti6Al-4V	4428	-	-	-	-	-	-0.09	0.27	0.48	0.014	3.87	[1]
1070 carbon steel	7800	-	-	-	-	-	0.05	0.8	-0.044	-0.046	0	[1]
Steel 4340	7830	1.67	4578	1.33	293.2	477	0.05	3.4	2.12	0	0.6	[8]
Al2017	2790	2	5328	1.34	293	875	-	-	-	-	-	[9]
Al6061-T651	2703	1.97	5240	1.4	293.2	885	-0.8	1.5	0.47	0	1.6	[10]
Al2024	-	1.97	5386	1.34	300	884	-	-	-	-	-	[11]
Al2024	2770	2	5330	1.34	-	875	-0.8	1.5	-0.5	0	1.6	[12]
7.62AP	7850	-	-	-	-	-	0.4	0	0	0	0	[15]
Al6061	2770	2	5350	1.34	293	875	-0.8	1.5	-0.5	0	1.6	[33]
Al	2770	-	-	-	293	875	-	-	-	-	-	[34]
Targets												
Al6061-T651	2703	1.97	5240	1.4	293.2	885	-0.77	1.45	0.47	0	1.6	[8]
Al2024-T81	2770	2	5330	1.34	293	875	-	-	-	-	-	[9]
Al5052	2680	2	5240	1.34	293	875	0.13	0.13	-1.5	0.011	0	[9]
Al6061-T6	2703	1.97	5240	1.4	293.2	885	-0.77	1.45	0.47	0	1.6	[10]
Al2024	-	1.97	5386	1.34	300	884	-	-	-	-	-	[11]
Mild steel	7850	-	-	-	-	-	0.1152	1.0116	- 1.7684	- 0.05279	0.5262	[15]
AISI-1045 steel	-	-	-	-	298	-	0.025	16.93	-14.8	0.0214	0	[18]
Armour steel	-	-	-	-	-	-	0.05	0.8	-0.44	-0.046	0	[19]
Al5052	2680	2	5350	1.34	293	875	0.13	0.1	-1.5	0.01	0	[33]
Al	2770	-	-	-	293	875	-	-	-	-	-	[34]

Mechanical properties of the projectiles and targets and their material constants based on literature are summarised in Table 3 [7-15, 18, 19, 22, 33, 34] and Table 4 [1, 8-12, 15, 17-19, 33, 34], respectively. Materials properties of the projectile and target in the current study were based on Ref [8] and [8, 9], respectively (Table 3, 4).

Part seeding was applied to deformable conical and blunt projectiles with an element size of 1mm, resulting in 12140 and 2900 C3D8R (Continuum 3D 8 node Reduced integration) elements, respectively, for Lagrangian parts. The SPH meshing slightly differed from standard element types such as C3D8R to simulate SPH bodies, as it required a particular element type, i.e., PC3D. The same element size as the projectile was selected to mesh SPH, and each element was divided into particles during analyses (by default, ABAQUS divides as per characteristic length, which is 0.5mm). Like SPH, CEL also requires a different element type, which is EC3D8R (Eulerian Continuum 3D 8 node Reduced integration) and an element size of 10mm. The Eulerian domain was constructed with a thickness of 100mm. A 1000µs time step was employed using a dynamic explicit solution. In all modelling techniques, circumferential surfaces of the plate were encastred. Self-interaction was considered between projectile and target elements, with a frictionless interaction property. A mesh convergence test was conducted on C3D8R elements. Default hourglass setup was established for projectile and target; element deletion was enabled for all cases. Kinetic energy, Johnson-Cook (JC) damage criteria, and velocities are requested as field output from the ABAQUS simulation. The following sections describe three modelling techniques and conditions applied in simulation.

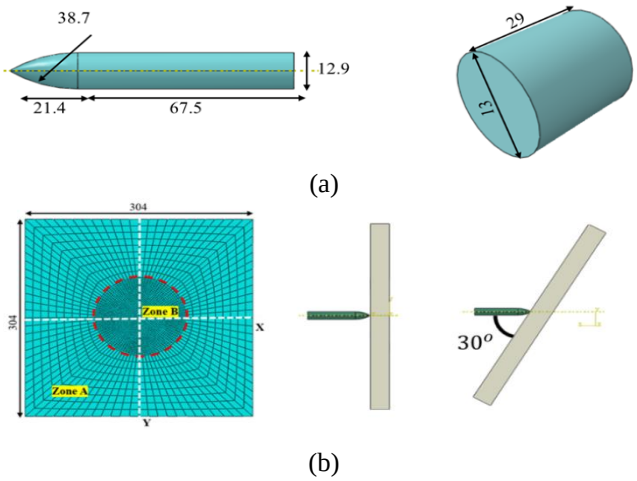

Figure 1, Projectile and target geometry, (a) dimensions of conical and blunt projectiles, (b) target dimensions, zones A, B for coarse and fine mesh, perpendicular (0°) and oblique (30°) impact assembly with a conical projectile (all dimensions in mm).

A. Lagrangian Model

Lagrangian modelling is a frequently used technique in Finite Element Method (FEM) to simulate static and dynamic problems. The Lagrangian method has material confined to a mesh which deforms with element deformation under stress (Figure 2a). Excessive mesh distortion of the elements associated with the contact interaction surface can limit the accuracy and strain rate, which can be accommodated in these models [7, 35]. For the current simulations, a target plate thickness of 26.3mm and an area of 304 mm^2 were considered (Figure 1). The target mesh is divided into zones A and B to reduce computational cost.

Retrieval Number: 100.1/ijeat.F452813060824
DOI: 10.35940/ijeat.F4528.13060824
Journal Website: www.ijeat.org

Published By:
Blue Eyes Intelligence Engineering and Sciences Publication (BEIESP)

Zone A mesh is defined by edge seeding of 24 on all four edges, and zone B has part seeding with an element size of 18mm, resulting in a total number of 5184 C3D8R elements. These dimensions were based on published literature, i.e., the geometry of the conical and blunt projectiles was adapted from [8] and from [13] for the blunt projectile, respectively, as shown in Figure 1.

B. Coupled Eulerian and Lagrangian

CEL offers an alternative to a Lagrangian model. i.e., The combination has an advantage in solving high-deformation problems as the Eulerian part has a fixed mesh where the material can flow in and out of the mesh [36, 37] (Figure 2a). In this method, the moments of continuum nodes are determined by Lagrangian mesh. The analysis uses Eulerian Volume Fraction (EVF). EVF=1 and EVF=0 specify that the mesh is filled with Eulerian and no material, respectively. It allows Lagrangian elements to move freely within the domain till interacting with the Eulerian part. It also allows the material to flow into "failed" elements because element deletion is turned off for Eulerian, and shear failure is not supported [38]. Figure 2a illustrates the difference between Lagrangian and Eulerian elements. An inflow boundary condition is assigned to the time step, which enables the Eulerian material to flow into the region and is controlled by inflow conditions across the specified region [38]. Eulerian material can easily interact with Lagrangian elements through Eulerian-Lagrangian contact; any analysis of these combinations is known as Coupled-Eulerian Lagrangian. The CEL method has been applied in high deformation, water sloshing, gas flows, and impact testing [17, 36, 37, 39, 40]. Some models are limited to volume fraction drag or thermal distribution due to the correlation of fraction on which dependence continued to volume fraction [41].

i. Johnson-Cook Plasticity Model

This analysis uses three methods to perform ballistic limits of thin aluminium plates with two projectile shapes. Both target and projectile are modelled using Johnson Cook and Mie-Grusiean (Equation of State, EOS), which are adapted from [25, 42], and the Von-mises flow stress σ is expressed in equation (1).

$$\sigma = [A + B\varepsilon^{n}][1 + Cln\dot{\varepsilon}^{*}][1 - T^{*m}] \ldots\ldots\ldots (1)$$

Where ε is the equivalent plastic strain, $\dot{\varepsilon}^{*} = \dot{\varepsilon}/\dot{\varepsilon}_{o}$, $\dot{\varepsilon}$ is the reference strain rate, $\dot{\varepsilon}^{*}$ is the plastic strain rate ($\dot{\varepsilon}_{0} = 1s^{-1}$) at an analogous temperature. A, B, n, C, and m are constants; the first bracket resolves the stress in the function of strain rate $\dot{\varepsilon}^{*} = 1$ and $T^{*} = 0$, $T^{*} = (T - T_{o})/(T_{m} - T_{o})$. The second and last square brackets define strain rate and temperature response.

The yield stress and strain hardening constant are B, n is the strain hardening coefficient [42], C is the strengthening strain rate, and m is the thermal softening coefficient.

It is suitable for high-strain deformation of various materials and is typically employed in adiabatic transient dynamic simulations. The damage criteria model accompanies the plasticity model, explained below [18, 25]. Table 5 gives some referred values for JC-plasticity and JC-failure constants from Ref [8, 9], which are used in this investigation.

ii. Johnson-Cook Failure Model

The Johnson-cook failure method is a general implementation of the damage initiation principle. It makes failure strain responsive to stress triaxiality, temperature, and strain rate. The JC model is based on the identical plastic strain at the particle integration point. Damage of the material is defined as: when D=0 there is no damage, D=1 failure occurs. JC failure model can be written as equation (2).

$$\varepsilon_{f} = \left[D_{1} + D_{2}exp\left(D_{3}\left(\frac{\sigma_{m}}{\sigma_{eq}}\right)\right)\right][1 + D_{4}ln(\dot{\varepsilon_{p}}^{*})][1 + D_{5}T^{*}] \ldots . (2)$$

Where $D_{1}\ to\ D_{5}$is the model constants and are primarily based on the equivalent plastic strain, stress triaxiality, temperature and strain rate., σ_{m} is the mean stress, $T^{*}$is the transition temperature, $\dot{\varepsilon_{p}}^{*}$is the plastic strain rate or effective strain rate, and σ_{eq} is the equivalent stress [18, 19] (Table 5). Failure elements are deleted within finite element code.

C. Smoothed Particle Hydrodynamics

Smoothed particle hydrodynamics (SPH) is based on the Lagrangian method. Mesh-free particles can be achieved by continuum equations interpolating the properties directly at a discrete set of points. This method was initially used to model astrophysical problems in three-dimensional space. Later, it was observed that the particle's movement was the same as gas or liquid and then modelled by Newtonian hydrodynamics [26, 43]. A set of particles with specific material properties interact with each other, which is controlled by the mass or smoothing function. SPH was obtained in two steps: 1) function and its derivates in continuous form as integral, also known as Kernel approximation in Figure 2(b), and 2) usually referred to as particle approximation. The first domain is discretised, illustrating elements representing the initial condition. Later, field factors on a molecule are approximated by adding the nearest acquaintance elements. The accuracy of the SPH model can be low [35], whereas Lagrangian exhibits high deformation. In a state of tensile stress, the molecule motion may fall in unstable conditions known as tensile instability, related to the interpolation approach of the standard SPH method. The surface loads, such as pressure, do not correspond to PC3D elements [43]. Converting to SPH particles is preferable to element deletion because the generated particles can provide deformation resistance above finite element distortion levels. As a result, element deletion and conversion are incompatible [44]. The Kernel function can be expressed as equation (3).

$$f(x) \cong \sum_{j}\frac{m_{j}}{\rho_{j}}f_{j}W(|x - x_{j}|, h) \ldots\ldots\ldots \quad (3)$$

The f(x) in equation (3) is further estimated by adding up the values of nearby particles. $W(|x - x_{j}|)$ is the Kernel function, a non-zero, m_{j} is the particle mass, ρ_{j} is the particle density, f_{j} is sampled through the sampling function (Kernel), and h is the smoothing length, denoted by subscript j (j refers to particles).

Similar analyses are based on Taylor series expansion, and Kernel approximation of the derivative is second-order accuracy. A Monte Carlo theory was used to convert discrete representation to obtain continuous representations of the spatial variations of two state variables. The particles are placed randomly from the mass distribution at first, but there was no significant error in particle density [45, 46]. The SPH method has relative advantages to other historic numerical practices utilising a network to discretise a problem. It can easily compromise with sophisticated dimensions and large-scale areas, sometimes lacking elements/particles [47].

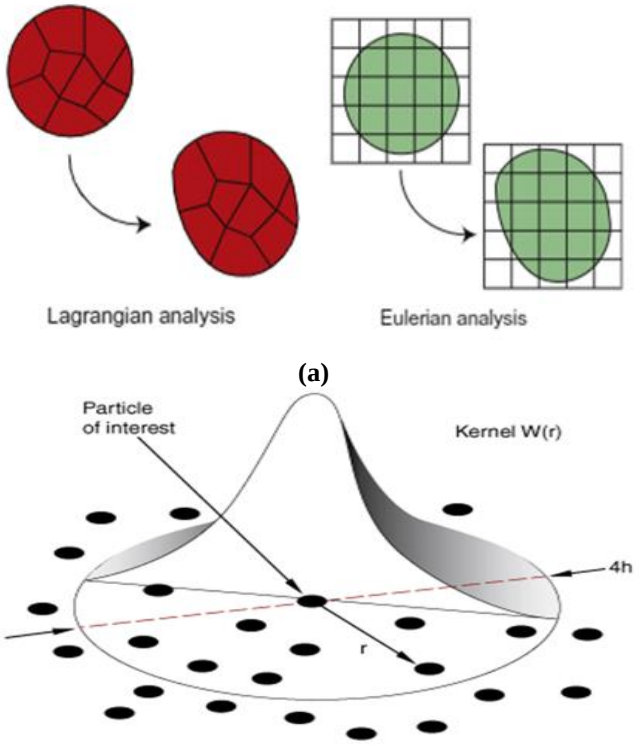

Figure 2, Model configurations, (a) difference between Lagrangian and Eulerian elements [40], (b) Kernel function for smoothed particle hydrodynamics (SPH) [43].

III. RESULTS AND DISCUSSION

A. Model Validation and Comparison of Modelling Techniques

Results of the steel projectile (4340) impacting an aluminium alloy of 6061-T651 for both perpendicular (0°) and oblique (30°) impact orientation (Table 2) are summarised in Figure 3(a, b).

These results are compared and validated with published experimental and numerical (Lagrangian) results in Ref [8].

Lagrangian results from the present study showed a good agreement with the numerical and experimental results of residual velocity [8], resulting in a 0 ∽ 6% error at various velocities (Figure 3a) above the ballistic limit.

At 800m/s, the error was 1%. For the SPH model, the error varied between 21% at a lower velocity of 400 m/s to 3% at 800m/s. The CEL model resulted in a higher error of 54% at the ballistic limit of 500 m/s to 21% at 800m/s. After the ballistic limit, the residual velocity showed a near-linear trend for an initial velocity range of 400-900m/s for the SPH and Lagrangian models. The trend for CEL was not near linear at a lower velocities, which is also evident from the higher %error for this model especially at lower initial velocity range. This is attributed to the fluid characteristics in CEL (Figure 2) where the contact interaction between Lagrangian and Eulerian part did not allow penetration of projectile until a relatively higher terminal velocity of 500 m/s when compared to the Lagrangian and SPH models. During low initial velocity impacts (<500m/s) for the CEL model, the projectile bounced back or recoiled, resulting in negative velocities and energies, as shown in Figure 3.

Published literature in Table 1 compares the range of %error for different modelling techniques for various projectiles and targets in the range of 4% to 40%. The %error of the current study (0% to 54%) for various modelling techniques is similar to the range in published literature. For example, based on the results summarised in Table 1, the % error for Lagrangian models vary between 4% to 38% [1, 8, 10, 11, 14, 15, 19-22, 24, 28, 30], whereas the %error ranges from 15∽ 20% for CEL [7, 17], 5∽ 25% for SPH [3, 9, 11-13, 17, 26, 28], 5%∽ 38% for experimental studies [16, 18, 23-25, 27, 31], 30∽ 40% for analytical techniques [2, 29, 32] and 22∽ 33% for few studies in published literature comparing the numerical modelling techniques [11, 18, 24, 28]. The trend between the initial velocity and residual velocity after the ballistic limit for the current study is also compared with other published studies for various projectile and target configurations [13, 15, 48, 49]. This is summarised in Figure 3 (c). This Figure shows that the published literature findings of the experimental and numerical investigations show a higher variance in results at lower initial velocities. This comparison indicates that for most published investigations and the current study, despite the difference in the shape, material and modelling techniques, the relationship between initial and residual velocity can be approximated as near-linear above ballistic limits and at initial velocities higher than 600 m/s.

B. Projectile and Target Interaction at Ballistic Limits

A comparison of the contour stress plots of projectile and target interaction between the three modelling techniques is shown in Figure 4 for oblique impacts at ballistic limits. Perpendicular impacts and blunt projectiles also showed a similar trend and were not shown here to avoid repetition. Few observations can be made from this comparison.

1) Significant projectile and target deformation is present in the CEL model, followed by projectile deformation in the Lagrangian and SPH models, respectively. The lower deformation of the projectile in the SPH model also resulted in the lowest ballistic limit, as shown in Figure 5 (a, b).

2) The extent of projectile deformation also dictated the target's damage or perforation, resulting in relatively higher target distortion for the CEL model (relatively higher in energy absorption for the CEL method compared to other models). Despite the higher ballistic limit for the CEL model, the target absorbed 88∽98% of projectile energy.

Retrieval Number: 100.1/ijeat.F452813060824
DOI: 10.35940/ijeat.F4528.13060824
Journal Website: www.ijeat.org

Published By:
Blue Eyes Intelligence Engineering and Sciences Publication (BEIESP)

3) The ballistic limits shown in Figure 5 (a, b) indicate that the ballistic limit is more influenced by the projectile shape compared to the modelling technique. Similarly, the impact angle has relatively less significant influence than the shape of the projectile and modelling technique at the ballistic limit. The percentage of the impact velocity residual at the ballistic limit varied between 24% to 79% depending upon the projectile shape, angle of impact and modelling technique.
4) The residual velocity at the ballistic limit follows the trend of Lagrangian → SPH → CEL for conical projectiles regardless of the angle of impact (Figure 5a). The projectile residual velocity at the ballistic limit is always higher for conical blunt projectiles, except for oblique impact for blunt CEL (Figure 5b).
5) For the conical projectiles, the energy absorbed for perforation at the ballistic limit decreases from CEL → Lagrangian → SPH for perpendicular impacts, whereas Lagrangian and SPH models show very similar results for oblique impact (Figure 5b). For blunt projectiles, Lagrangian and SPH models show very similar results in terms of %energy absorbed regardless of the impact angle.

T. Borvik et al.[30] studied the ballistic testing on AA6082-T4 aluminium plate using arm bullets with obliquity from 0-60° increment of 15° for each test and velocity of 830m/s. Results from the current study for oblique (30°) impact angle showed similar relations for current oblique impact for the Lagrangian conical projectile.

The same Lagrangian projectile was used for SPH impact simulation without altering the element type. However, zone B elements of the AA6061-T651 plate (Figure 1) are converted to discrete elements. Generally, the size of the discrete particle is half of the mesh density within the region with unconstrained particles, which means that it can interact with Lagrangian bodies and other particles. Similarly, Palmieri et al. [28] tested an aluminium Whipple shield bumper using SPH hydrocodes using AUTODYN and Pam-shock and compared it with NASA ballistic curves; pam-shock overestimated the NASA results. Perpendicular impact presented a higher advantage in perforating the plate than the oblique. The ballistic limit for both impact angles (perpendicular and oblique) is Vb =300m/s. Changing plate orientation from perpendicular to oblique resulted in approximately a 2.85% increase in energy absorption (Figure 5).

C. Influence of Modelling Method, Projectile Shape, and Target Thickness

i. Lagrangian Configuration - Projectile Shape, Plate Material and Thickness

Figure 6 summarises the influence of target material (AA6061-T651 and Al5052) and target thickness (16 mm, 20 mm, 26.3 mm) for AA6061-T651 plate on the ballistic limit and residual velocity for a conical projectile in perpendicular impacts.

The ballistic limit for the AA6061-T651 was higher (Vb = 400m/s) when compared to the Al5052 plate (Vb = 300m/s). This difference is attributed to the higher strength of the material (approximately 18% higher yield strength.). The change of plate thickness from 16 mm to 20 mm did not influence the ballistic limit (Vb = 300 m/s), whereas 26.3 mm thickness indicated a higher ballistic limit (Vb = 400 m/s). Despite these differences in the ballistic limits due to plate thickness and material changes, there was a near-linear trend between the initial and residual velocity. Furthermore, at velocities higher than 600 m/s, the influence of plate material and thickness on the residual velocity was negligible. This is because the proportion of projectile initial energy absorbed by the target decreases at higher initial velocities (Figures 5, 6).

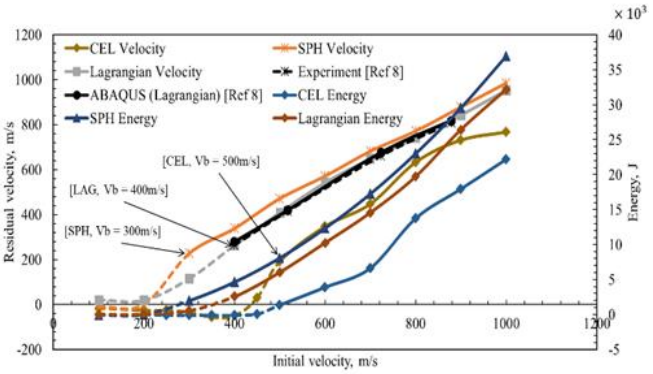

(a)

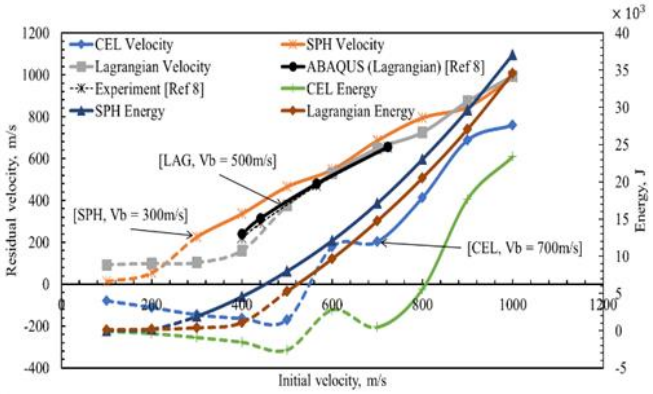

(b)

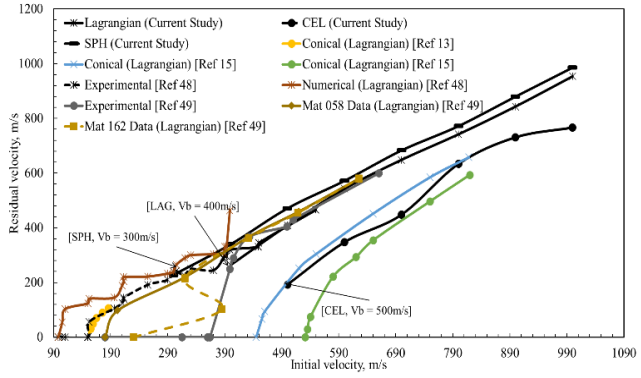

(c)

Figure 3, Initial and residual velocity plots for a deformable conical projectile using Lagrangian (LAG), SPH and CEL modelling techniques from current investigation and its Comparison with results in Ref [8], (a) perpendicular projectile, (b) oblique (30°) impact, (c) comparison of results with Refs [13,15,48,49]. The ballistic limit (Vb) is also indicated for each model, and the negative velocity and energy show projectile recoil.

Retrieval Number: 100.1/ijeat.F452813060824
DOI: 10.35940/ijeat.F4528.13060824
Journal Website: www.ijeat.org

Published By:
Blue Eyes Intelligence Engineering and Sciences Publication (BEIESP)

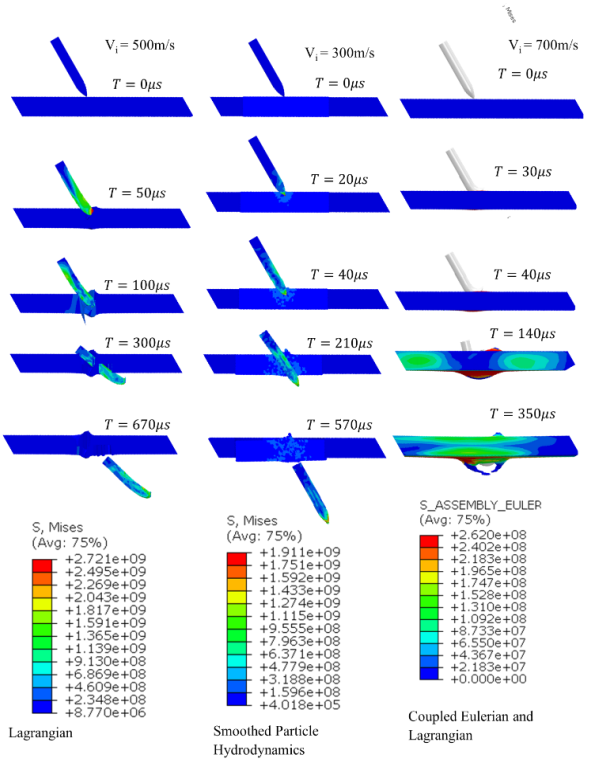

Figure 4, A comparison of contour plots and plastic deformation for conical projectiles at the ballistic limits for three modelling techniques for oblique impact. The maximum Von Mises stress (Pa) was observed in the projectile regardless of the modelling technique; the results for CEL show the stress only in the target.

ii. Modelling Method and Projectile Shape

Figure 7 compares the modelling techniques for conical and blunt projectiles above the ballistic limit. The ballistic limits for each modelling technique and projectile shape are also shown in the Figure. The following observations can be made from the analysis of this Figure.

1) Regardless of the change in projectile shape, there is a near-linear relationship between the initial and residual velocity above the ballistic limit. This is consistent with the observation in Figures. 3 to 6, where the change in modelling technique, target plate material and thickness also indicated this near-linearity above the ballistic limit.

2) The projectile shape more significantly influences the ballistic limit than the change in the modelling technique.

The above can be observed from the change in ballistic limit from conical to blunt projectile of 400 m/s to 800 m/s (100% increase) for the Lagrangian, 300 m/s to 500 m/s (66% increase) for SPH and 500 m/s to 1000 m/s (increase of 100%) for the CEL models. When comparing the changes in the ballistic limits due to the changes in modelling technique, there is an increase of ballistic limit for a conical projectile of 300 m/s for SPH to 500 m/s for the CEL when compared to Lagrangian model at 400m/s (% change of ± 25% when compared to Lagrangian). Blunt projectile showed a similar trend (% change of -28% and + 43% compared to Lagrangian). A similar trend can be observed when comparing the angle of impact summarised in Figure 5. These findings are consistent with the influence of local and longitudinal impact structures consuming the projectile's kinetic energy [27].

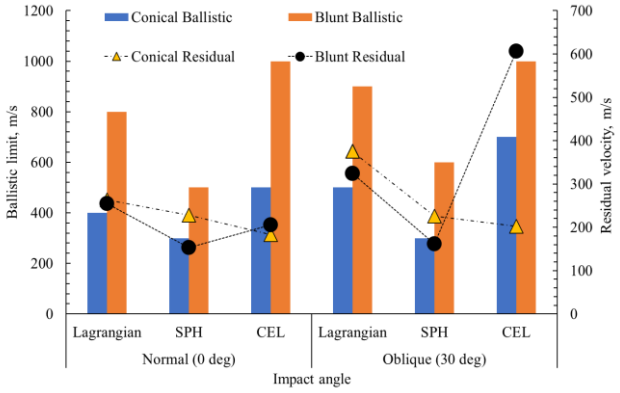

(a)

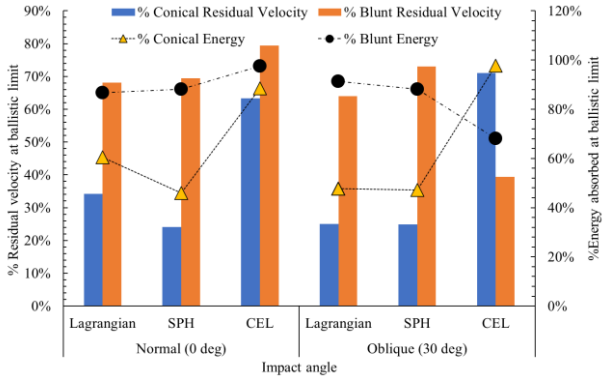

(b)

Figure 5, Analysis of ballistic limits, angle of impact and projectile shape for three modelling techniques, (a) ballistic limit and residual velocity, (b) % of residual velocity [(Vi-Vb)×100/Vi] and energy [(Ei-Eb)×100/Ei] absorbed at the ballistic limit.

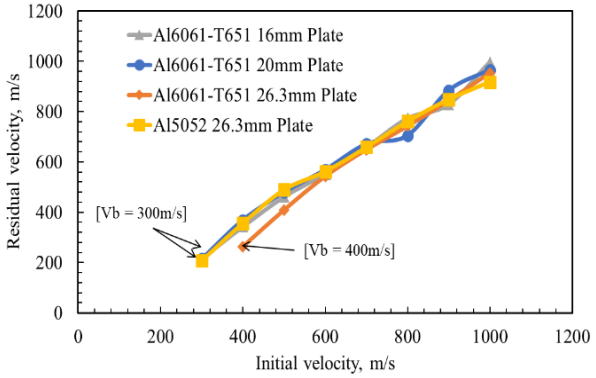

Figure 6, Comparison of initial and residual velocity for three plate thicknesses and two different plate materials using the Lagrangian model for perpendicular impact. The arrows indicate the ballistic limit (Vb) for each case.

D. Rigid and Deformable Projectiles

Using rigid projectiles can reduce 1) computing effort and 2) excessive mesh deformation issues when modelling the contact interaction [35].

This can, however, result in a reduction in the model's

Retrieval Number: 100.1/ijeat.F452813060824
DOI: 10.35940/ijeat.F4528.13060824
Journal Website: www.ijeat.org

Published By:
Blue Eyes Intelligence Engineering and Sciences Publication (BEIESP)

accuracy; nevertheless, there is a tradeoff between them. This section considers this analysis to understand the influence of switching the projectile from deformable to rigid. Projectile mass was incorporated by converting the conical projectile into an analytical rigid with a point mass of 81.1g to match the specification of the deformable projectile used in the previous simulation. X. Chen et al. [2] derived a prediction formula using experimental data and rigid projectiles on thick plates on 6061-T651 aluminium 0º and 30º projection orientation. His study reveals that the perforation of a thick plate is influenced by various non-dimensional factors such as impact function, projectile geometry, target thickness, and impact obliquity. These formulae can be applied to various nose shapes and target materials using dynamic cavity theory. A comparison of results from the current study is summarised in Figure 8. The following observations can be made from this analysis.

1) The ballistic limit remains unchanged for the conical projectiles for deformable and rigid configurations. A rigid conical projectile slightly overestimates the residual velocity above the ballistic limit. The percentage difference between the results of residual velocity ranged from 20% at the lower initial velocity of 400 m/s to 2% at the higher initial velocity of 800 m/s. In terms of computing effort, there was a 55% reduction in computing time when switching to a rigid indenter. A similar trend was observed for the SPH and CEL models.

2) For the blunt projectiles, switching to a rigid configuration in the Lagrangian model underestimates the ballistic limit as it is reduced from 800m/s to 400 m/s. This is because, whilst the conical projectile shape is designed to penetrate the target with minimum distortion, the blunt projectile has to deform considerably as it goes through the target. Qualitatively, this can be used to approximate the proportion of energy absorbed by the projectile, which will be about ∽50%. A similar trend was observed for the SPH model, where the rigid blunt indenter underestimates the ballistic limit (from 500 m/s to 400 m/s). This shows that the energy associated with projectile deformation is relatively lower in SPH compared to the Lagrangian model, which is consistent with the observations from Figures 4 to 8. Apart from changes in the ballistic limit, the relationship between the residual velocity and initial velocity after the ballistic limit remains near-linear, consistent with the findings in the above sections.

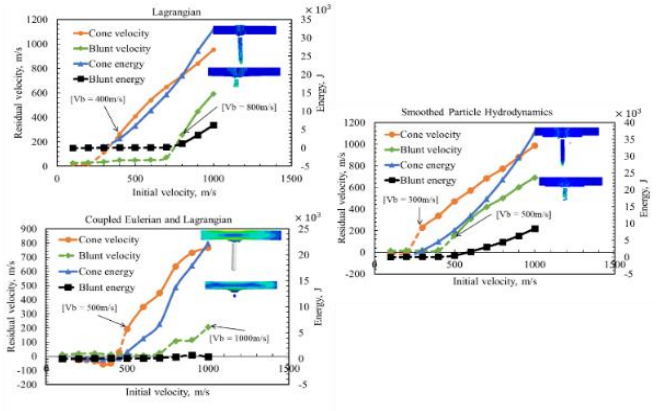

Figure 7, Comparison of Lagrangian, SPH, and CEL residual velocities and energies at different projectile velocities for conical projectiles for perpendicular impact. The arrows indicate the ballistic limit (Vb) for each case.

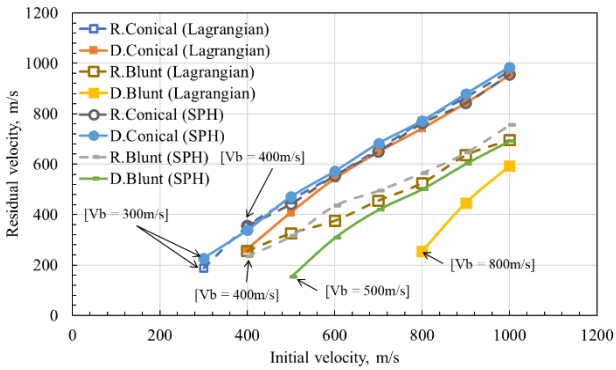

Figure 8, Comparison of deformable (D.) and rigid (R.) conical and blunt projectiles on the residual velocity and ballistic limit (Vb) for Lagrangian and SPH models.

E. Comparison of Modelling Techniques

The Lagrangian approach is popular for simulating high-velocity impacts when comparing the three modelling configurations. It has the advantage of using axisymmetric modelling, which can considerably reduce computation time [35]. This approach, however, has a drawback as it may result in a lower accuracy and convergence issues due to severe distortions in the deformed area [56]. High plastic strain rate, particle rebound, and unrealistic deformation can suffer from excessive mesh distortion, often resulting in program termination [35, 57]. Arbitrary Lagrangian Eulerian (ALE) adaptive re-meshing can sometimes be used to overcome mathematical truncation errors caused by severely distorted elements [35]. The current study's velocity range of 100 to 1000 m/s did not cause severe mesh distortion and termination; however, this can pose modelling issues at hypervelocities, e.g., in space applications where the velocities are ∽30km/s.

The Coupled Eulerian-Lagrangian (CEL) approach offers greater flexibility and better results than the Eulerian method alone, especially when strain rate and mesh distortion exceed the capabilities of the Lagrangian model [37]. Eulerian analysis allows material to withstand high mesh distortion compared to the Lagrangian model. As a result, it is important to specify the material behaviour for the entire strain range, which frequently requires defining a failure behaviour. The CEL formulation involves subjecting every material within the element to the same strain level and then enabling the stress and other state details to develop separately within each material. During simulation, the Lagrangian body forces the material out of the Eulerian elements it passes through, making a void. This interaction resulted in a higher projectile deformation and ballistic limit in the current investigation (Figures 4, 5). On the other hand, the flow of Eulerian material towards the Lagrangian body is halted from entering the underlying Eulerian elements. However, there are limitations to the CEL method, i.e.: a) Failure models associated with shear are not supported, b) The constraints of Eulerian-Lagrangian contact are implemented through penalty method, in which the stiffness parameter for penalty is automatically optimised within the limits of stability,

Retrieval Number: 100.1/ijeat.F452813060824
DOI: 10.35940/ijeat.F4528.13060824
Journal Website: www.ijeat.org

Published By:
Blue Eyes Intelligence Engineering and Sciences Publication (BEIESP)

c) It is not possible to apply non-zero displacement boundary conditions to Eulerian nodes, d) In certain scenarios Eulerian material can infiltrate the Lagrangian contact surface near sharp corners [37, 38].

SPH method is used to solve a continuous problem in a Lagrangian reference frame. This approach involves using discrete particles to carry information, and it uses a smoothing Kernel function to interpolate the values of the continuum fields. The neighbouring particles are summed up in this meshless technique to obtain the interpolated values [58]. SPH methods are frequently used in hypervelocity (≥ 1000m/s) studies to observe micro space debris, micro meteoroids, plastic deformation of metallic plates and spacecraft inner wall perforation [9, 12, 26, 59, 60]. SPH formulation may not capture certain physical phenomena critical in high-speed impact simulations, such as shock waves and material failure. However, it has limitations: a) Boundary conditions are invalid or cannot be applied to generated particles, b) The interaction between smoothed particle hydrodynamic bodies is significant only when made of the same fluid-like material. However, when dealing with solids-related applications, such as simulating a bullet penetrating an armour plate, one of the bodies must be represented using regular finite elements to define contact interactions. c) It is not possible to establish contact interactions between Eulerian regions and particles. d) The way mass is distributed in a body defined by particle elements is not the same as in a body defined by continuum elements, specifically C3D8R elements [43, 44].

Due to this, SPH may result in less model accuracy when there is no severe deformation compared to other methods, such as Lagrangian. PC3D elements are not equipped with faces or edges, so there are no forces related to hourglass or distortion control associated with them [57]. In numerical methods, artificial energy is utilised to prevent nonphysical deformation caused by reduced integration elements. This energy is mainly dissipated to control hour glassing deformation [57]. Hence, in the velocity range of 100 to 1000m/s considered in this study, SPH model slightly underestimated the ballistic limit, however, this method can overcome high strain rate and mesh distortion issues in hypervelocity models.In addition to the above modelling techniques, other methods have also been attempted in the published literature. The material point method (MPM) combines features of Lagrangian and Eulerian methods. In this technique, the materials are represented by material points that move with the materials while the computational grid remains fixed. MPM is an effective method for simulating large deformations, material fragmentation, and contact-impact problems. It is widely used to analyse impact events in geomechanics, structural dynamics, and biomechanics. However, interpreting this method requires mixed Lagrangian and Eulerian strategies, which makes it similar to most other methods [50]. The Element-Free Galerkin Method (EFG) is a mesh-less approach that uses the Galerkin weak formulation of the governing equations. Instead of requiring the mesh to follow the geometry or material interfaces, EFG relies on a background mesh for numerical integration. This method only needs nodal data and does not require element connectivity. In a previous version of EFG, Lagrange multipliers were utilised to enforce essential boundary conditions. EFG is a suitable method for problems that involve large deformations, material interfaces, and contact impact, making it applicable for high-speed impact simulations [51]. The discrete element method (DEM) was developed to describe granular materials by directly solving individual particles' movements. In the classical DEM, spherical shapes are used to model particles. The MPM/DEM method combines MPM with DEM, simulating continuous and discreet materials in the same framework. This technique suits problems involving granular materials, particle-fluid interactions, and soil-structure interaction under high-speed impact conditions [52]. The Generalized Finite Element Method (GFEM) is an upgraded version of the traditional finite element approximations. It includes additional degrees of freedom to capture localised phenomena such as cracks, interfaces, or discontinuities. The GFEM has several vital features. Firstly, it allows for essential boundary conditions to be imposed precisely as in the standard FEM, which is not possible in other partition of unity-based methods. Secondly, the accuracy of numerical integration is controlled adaptively to prevent errors from affecting the accuracy of the approximation. This is an issue that has not been addressed adequately in other methods. Finally, linear dependencies in the system of equations are resolved using a simple modification of the direct linear solver. GFEM is particularly useful for simulating material failure, fragmentation, and crack propagation in high-speed impact scenarios [53]. The Particle Finite Element Method (PFEM) is a mathematical method designed to solve problems that involve large deformations of an area and multiple physical phenomena. Initially, it was created to deal with the interaction between fluid and solid structures, particularly in free-surface flows. The method uses Gaussian points or nodes that act as particles and carry physical information to address mesh distortion issues by re-meshing with Delaunay triangulation. The PFEM combines the benefits of mesh-based techniques' precision and resilience with particle-based methods. It divides the physical area into a mesh where the governing differential equations are solved using a standard finite element approach. This method suits problems involving fluid-structure interactions, free surface flows, and material fragmentation. It can accurately model the intricate behaviour of materials that undergo high-speed impact conditions [52, 54, 55].

IV. CONCLUSION

A ballistic limit simulation was performed on a 26.3mm thick aluminium 304 mm^2 plate utilising two different projectiles in three distinctive model configurations. The key findings of this investigation are as follows.

1. In the Lagrangian model the conical projectile showed a higher ballistic limit for AA6061-T651 (Vb=400m/s) compared to the Al5052 (Vb=300m/s) plate during perpendicular impact.
2. Changing plate orientation from perpendicular to oblique resulted in a 20% (Vb=500m/s) high ballistic limit for a deformable conical projectile in the Lagrangian model. A similar trend followed for deformable blunt projectile Vb=800m/s and Vb=900m/s for perpendicular and oblique impacts, respectively.

Retrieval Number: 100.1/ijeat.F452813060824
DOI: 10.35940/ijeat.F4528.13060824
Journal Website: www.ijeat.org

Published By:
Blue Eyes Intelligence Engineering and Sciences Publication (BEIESP)

3. In SPH modelling, the ballistic limit for the conical projectile is unchanged regardless of target plate orientation. However, the ballistic limit for blunt projectile exhibited lower velocity (Vb=500m/s) for perpendicular orientation and higher (Vb=600m/s) for oblique orientation.
4. During CEL modelling, the conical projectile showed a nearly 28% increase in the ballistic limit for oblique orientation (Vb=700m/s) than perpendicular (Vb=500m/s). Blunt projectile showed the same ballistic limit as conical projectile in SPH modelling.
5. A near-linear trend existed between the initial and residual velocity above the ballistic limits.
6. Perforation energy absorbed at the ballistic limit decreases from CEL → Lagrangian → SPH for perpendicular conical impacts. For blunt projectiles, Lagrangian and SPH models show very similar results in terms of %energy absorbed regardless of the impact angle.
7. The rigid projectile in the Lagrangian model showed high residual velocity but the same ballistic limit of 400m/s for perpendicular impact.

A similar trend was observed for the SPH model. In contrast to the conical, the blunt rigid projectile exhibited lower residual velocity.

DECLARATION STATEMENT

Funding	No, We did not receive any financial support for this article.
Conflicts of Interest	No conflicts of interest to the best of our knowledge.
Ethical Approval and Consent to Participate	No, the article does not require ethical approval and consent to participate with evidence.
Availability of Data and Material	Not relevant.
Authors Contributions	All authors have equal contributions of this article.

REFERENCES

1. S. Shasthri and V. Kausalyah, "Effect of ballistic impact on Ti6Al-4V titanium alloy and 1070 carbon steel bi-layer armour panel," *International journal of structural integrity*, vol. 11, no. 4, pp. 557-565, 2020, doi: 10.1108/IJSI-09-2019-0095. https://doi.org/10.1108/IJSI-09-2019-0095
2. F. Xiaowei Chen Qingming Li Saucheong, "Oblique perforation of thick metallic plates by rigid projectiles," *Acta mechanica Sinica*, vol. 22, no. 4, pp. 367-376, 2006, doi: 10.1007/s10409-006-0015-8. https://doi.org/10.1007/s10409-006-0015-8
3. Y. Zhou, Y. Sun, and T. Huang, "SPH-FEM Design of Laminated Plies under Bird-Strike Impact," *Aerospace*, vol. 6, no. 10, p. 112, 2019. https://doi.org/10.3390/aerospace6100112
4. P. R. Gradl and W. Stephens, "Space Shuttle Main Engine Debris Testing Methodology and Impact Tolerances," ed, 2005. https://doi.org/10.2514/6.2005-3628
5. J. Gabrys, K. Carney, E. L. Fasanella, M. Melis, and K. H. Lyle, "Test and Analysis Correlation of Form Impact onto Space Shuttle Wing Leading Edge RCC Panel 8," ed, 2004.
6. C. A. Myhre, S. R. Best, and R. J. Christie, "Hypervelocity Impact Testing of Space Station Freedom Solar Cells," ed, 1994.
7. A. Fardan and R. Ahmed, "Modeling the Evolution of Residual Stresses in Thermally Sprayed YSZ Coating on Stainless Steel Substrate," 2019. https://doi.org/10.1007/s11666-019-00856-2
8. D. Systems. "Simulation of the ballistic perforation of aluminum plates with Abaqus/Explicit." https://www.3ds.com/fileadmin/PRODUCTS-SERVICES/SIMULIA/RESOURCES/aero-ballistic-perforation-alumnium-plates-12.pdf (accessed 22 September, 2020).
9. P. Liu, Y. Liu, and X. Zhang, "Improved shielding structure with double honeycomb cores for hyper-velocity impact," *Mechanics research communications*, vol. 69, pp. 34-39, 2015, doi: 10.1016/j.mechrescom.2015.06.003. https://doi.org/10.1016/j.mechrescom.2015.06.003
10. A. Dorogoy, D. Rittel, and D. Weihs, "Effect of target velocity on damage patterns in hypervelocity glancing collisions," *International Journal of Impact Engineering*, vol. 144, p. 103664, 2020/10/01/ 2020, doi: https://doi.org/10.1016/j.ijimpeng.2020.103664.
11. X. Zhang, T. Liu, X. Li, and G. Jia, "Hypervelocity impact performance of aluminum egg-box panel enhanced Whipple shield," *Acta astronautica*, vol. 119, pp. 48-59, 2016, doi: 10.1016/j.actaastro.2015.10.013. https://doi.org/10.1016/j.actaastro.2015.10.013
12. P. Liu, Y. Liu, X. Zhang, and Y. Guan, "Investigation on high-velocity impact of micron particles using material point method," *International journal of impact engineering*, vol. 75, pp. 241-254, 2015, doi: 10.1016/j.ijimpeng.2014.09.001. https://doi.org/10.1016/j.ijimpeng.2014.09.001
13. M. Rodriguez-Millan, D. Garcia-Gonzalez, A. Rusinek, F. Abed, and A. Arias, "Perforation mechanics of 2024 aluminium protective plates subjected to impact by different nose shapes of projectiles," *Thin-walled structures*, vol. 123, pp. 1-10, 2018, doi: 10.1016/j.tws.2017.11.004. https://doi.org/10.1016/j.tws.2017.11.004
14. T. Fras, L. Colard, E. Lach, A. Rusinek, and B. Reck, "Thick AA7020-T651 plates under ballistic impact of fragment-simulating projectiles," *International journal of impact engineering*, vol. 86, pp. 336-353, 2015, doi: 10.1016/j.ijimpeng.2015.08.001. https://doi.org/10.1016/j.ijimpeng.2015.08.001
15. M. A. Iqbal, K. Senthil, P. Bhargava, and N. K. Gupta, "The characterisation and ballistic evaluation of mild steel," *International journal of impact engineering*, vol. 78, pp. 98-113, 2015, doi: 10.1016/j.ijimpeng.2014.12.006. https://doi.org/10.1016/j.ijimpeng.2014.12.006
16. A. J. Piekutowski, M. J. Forrestal, K. L. Poormon, and T. L. Warren, "Perforation of aluminum plates with ogive-nose steel rods at normal and oblique impacts," *International journal of impact engineering*, vol. 18, no. 7-8, pp. 877-887, 1996, doi: 10.1016/s0734-743x(96)00011-5. https://doi.org/10.1016/S0734-743X(96)00011-5
17. I. Smojver and D. Ivančević, "Bird strike damage analysis in aircraft structures using Abaqus/Explicit and coupled Eulerian Lagrangian approach," *Composites science and technology*, vol. 71, no. 4, pp. 489-498, 2011, doi: 10.1016/j.compscitech.2010.12.024. https://doi.org/10.1016/j.compscitech.2010.12.024
18. M. Murugesan and D. Jung, "Johnson Cook Material and Failure Model Parameters Estimation of AISI-1045 Medium Carbon Steel for Metal Forming Applications," *Materials*, vol. 12, no. 4, p. 609, 2019, doi: 10.3390/ma12040609. https://doi.org/10.3390/ma12040609
19. A. Banerjee, S. Dhar, S. Acharyya, D. Datta, and N. Nayak, "Determination of Johnson cook material and failure model constants and numerical modelling of Charpy impact test of armour steel," *Materials science & engineering. A, Structural materials : properties, microstructure and processing*, vol. 640, pp. 200-209, 2015, doi: 10.1016/j.msea.2015.05.073. https://doi.org/10.1016/j.msea.2015.05.073
20. A. F. Johnson, A. K. Pickett, and P. Rozycki, "Computational methods for predicting impact damage in composite structures," *Composites science and technology*, vol. 61, no. 15, pp. 2183-2192, 2001, doi: 10.1016/S0266-3538(01)00111-7. https://doi.org/10.1016/S0266-3538(01)00111-7
21. J. Jovicic, A. Zavaliangos, and F. Ko, "Modeling of the ballistic behavior of gradient design composite armors," *Composites. Part A, Applied science and manufacturing*, vol. 31, no. 8, pp. 773-784, 2000, doi: 10.1016/s1359-835x(00)00028-2. https://doi.org/10.1016/S1359-835X(00)00028-2
22. X. Chen, Y. Peng, S. Peng, S. Yao, C. Chen, and P. Xu, "Flow and fracture behavior of aluminum alloy 6082-T6 at different tensile strain rates and triaxialities," *PloS one*, vol. 12, no. 7, p. e0181983, 2017, doi: 10.1371/journal.pone.0181983. https://doi.org/10.1371/journal.pone.0181983
23. D. C. Hofmann, L. Hamill, E. Christiansen, and S. Nutt, "Hypervelocity Impact Testing of a Metallic Glass-Stuffed Whipple Shield," *Advanced engineering materials*, vol. 17, no. 9, pp. 1313-1322, 2015, doi: 10.1002/adem.201400518. https://doi.org/10.1002/adem.201400518
24. S. Signetti, F. Bosia, S. Ryu, and N. M. Pugno, "A combined experimental/numerical study on the scaling of impact strength and toughness in composite laminates for ballistic applications," *Composites. Part B, Engineering*, vol. 195, p. 108090, 2020, doi:

10.1016/j.compositesb.2020.108090. https://doi.org/10.1016/j.compositesb.2020.108090
25. G. R. Johnson and W. H. Cook, "Fracture characteristics of three metals subjected to various strains, strain rates, temperatures and pressures," *Engineering fracture mechanics*, vol. 21, no. 1, pp. 31-48, 1985. https://doi.org/10.1016/0013-7944(85)90052-9
26. M. B. Liu and G. R. Liu, "Smoothed Particle Hydrodynamics (SPH): an Overview and Recent Developments," *Archives of computational methods in engineering state of the art reviews.*, vol. 17, no. 1, pp. 25-76, 2010, doi: 10.1007/s11831-010-9040-7. https://doi.org/10.1007/s11831-010-9040-7
27. M. Rodríguez-Millán, A. Vaz-Romero, A. Rusinek, J. A. Rodríguez-Martínez, and A. Arias, "Experimental Study on the Perforation Process of 5754-H111 and 6082-T6 Aluminium Plates Subjected to Normal Impact by Conical, Hemispherical and Blunt Projectiles," *Experimental mechanics*, vol. 54, no. 5, pp. 729-742, 2014, doi: 10.1007/s11340-013-9829-z. https://doi.org/10.1007/s11340-013-9829-z
28. D. Palmieri, M. Faraud, R. Destefanis, and M. Marchetti, "Whipple shield ballistic limit at impact velocities higher than 7 km/s," *International journal of impact engineering*, vol. 26, no. 1, pp. 579-590, 2001, doi: 10.1016/S0734-743X(01)00118-X. https://doi.org/10.1016/S0734-743X(01)00118-X
29. A. Nuttall and S. Close, "A thermodynamic analysis of hypervelocity impacts on metals," *International journal of impact engineering*, vol. 144, no. C, p. 103645, 2020, doi: 10.1016/j.ijimpeng.2020.103645. https://doi.org/10.1016/j.ijimpeng.2020.103645
30. T. Børvik, L. Olovsson, S. Dey, and M. Langseth, "Normal and oblique impact of small arms bullets on AA6082-T4 aluminium protective plates," *International journal of impact engineering*, vol. 38, no. 7, pp. 577-589, 2011, doi: 10.1016/j.ijimpeng.2011.02.001. https://doi.org/10.1016/j.ijimpeng.2011.02.001
31. J.-H. Cha, Y. Kim, S. K. Sathish Kumar, C. Choi, and C.-G. Kim, "Ultra-high-molecular-weight polyethylene as a hypervelocity impact shielding material for space structures," *Acta Astronautica*, vol. 168, pp. 182-190, 2020/03/01/ 2020, doi: https://doi.org/10.1016/j.actaastro.2019.12.008.
32. W. Schonberg, F. Schäfer, and R. Putzar, "Hypervelocity impact response of honeycomb sandwich panels," *Acta astronautica*, vol. 66, no. 3-4, pp. 455-466, 2010, doi: 10.1016/j.actaastro.2009.06.018.
33. P. Liu, Y. Liu, and X. Zhang, "Internal-structure-model based simulation research of shielding properties of honeycomb sandwich panel subjected to high-velocity impact," *International journal of impact engineering*, vol. 77, pp. 120-133, 2015, doi: 10.1016/j.ijimpeng.2014.11.004.
34. J. M. Sibeaud, L. Thamié, and C. Puillet, "Hypervelocity impact on honeycomb target structures: Experiments and modeling," *International journal of impact engineering*, vol. 35, no. 12, pp. 1799-1807, 2008, doi: 10.1016/j.ijimpeng.2008.07.037. https://doi.org/10.1016/j.ijimpeng.2008.07.037
35. A. Fardan, C. C. Berndt, and R. Ahmed, "Numerical modelling of particle impact and residual stresses in cold sprayed coatings: A review," *Surface & coatings technology*, vol. 409, p. 126835, 2021, doi: 10.1016/j.surfcoat.2021.126835. https://doi.org/10.1016/j.surfcoat.2021.126835
36. S. Jeong and K. Lee, "Analysis of the impact force of debris flows on a check dam by using a coupled Eulerian-Lagrangian (CEL) method," *Computers and geotechnics.*, vol. 116, p. 103214, 2019, doi: 10.1016/j.compgeo.2019.103214. https://doi.org/10.1016/j.compgeo.2019.103214
37. P. Benson. "Eulerian Analysis." https://abaqus-docs.mit.edu/2017/English/SIMACAEANLRefMap/simaanl-c-eulerianananalysis.htm (accessed 2021).
38. [38] ABAQUS/Explicit. "Eulerian Analysis." https://abaqus-docs.mit.edu/2017/English/SIMACAEANLRefMap/simaanl-c-eulerianananalysis.htm#simaanl-c-aeuleriananal-bc (accessed 2021).
39. S. Heimbs, "Computational methods for bird strike simulations: A review," *Computers & structures*, vol. 89, no. 23-24, pp. 2093-2112, 2011, doi: 10.1016/j.compstruc.2011.08.007. https://doi.org/10.1016/j.compstruc.2011.08.007
40. G. Qiu, S. Henke, and J. Grabe, "Application of a Coupled Eulerian–Lagrangian approach on geomechanical problems involving large deformations," *Computers and geotechnics.*, vol. 38, no. 1, pp. 30-39, 2011, doi: 10.1016/j.compgeo.2010.09.002. https://doi.org/10.1016/j.compgeo.2010.09.002
41. S. Subramaniam, "Lagrangian–Eulerian methods for multiphase flows," *Progress in energy and combustion science*, vol. 39, no. 2-3, pp. 215-245, 2013, doi: 10.1016/j.pecs.2012.10.003. https://doi.org/10.1016/j.pecs.2012.10.003
42. G. R. Johnson, "A constitutive model and data for materials subjected to large strains, high strain rates, and high temperatures," *Proc. 7th Inf. Sympo. Ballistics*, pp. 541-547, 1983.
43. Abaqus/Explicit, "Smoothed particle hydrodynamics," ed.
44. ABAQUS/Explicit. "SPH." https://abaqus-docs.mit.edu/2017/English/SIMACAEANLRefMap/simaanl-c-sphconversion.htm (accessed 2021).
45. L. B. Lucy, "A numerical approach to the testing of the fission hypothesis," *The astronomical journal*, vol. 82, pp. 1013-1024, 1977. https://doi.org/10.1086/112164
46. R. A. Gingold and J. J. Monaghan, "Smoothed particle hydrodynamics: theory and application to non-spherical stars," *Monthly notices of the royal astronomical society*, vol. 181, no. 3, pp. 375-389, 1977. https://doi.org/10.1093/mnras/181.3.375
47. F. Chaari, *Advances in materials, mechanics and manufacturing : proceedings of the second International Conference on Advanced Materials, Mechanics and Manufacturing (A3M'2018), December 17-19, 2018 Hammamet, Tunisia / Fakher Chaari [and six others] editors*, 1st ed. 2020. ed. Cham, Switzerland : Springer, 2020.
48. B. L. Buitrago, C. Santiuste, S. Sánchez-Sáez, E. Barbero, and C. Navarro, "Modelling of composite sandwich structures with honeycomb core subjected to high-velocity impact," *Composite structures*, vol. 92, no. 9, pp. 2090-2096, 2010, doi: 10.1016/j.compstruct.2009.10.013. https://doi.org/10.1016/j.compstruct.2009.10.013
49. R. Scazzosi, A. Manes, and M. Giglio, "An Enhanced Material Model for the Simulation of High-Velocity Impact on Fiber-Reinforced Composites," *Procedia Structural Integrity*, vol. 24, pp. 53-65, 2019/01/01/ 2019, doi: https://doi.org/10.1016/j.prostr.2020.02.005.
50. M. Steffen, R. M. Kirby, and M. Berzins, "Analysis and reduction of quadrature errors in the material point method (MPM)," *International journal for numerical methods in engineering*, vol. 76, no. 6, pp. 922-948, 2008, doi: 10.1002/nme.2360. https://doi.org/10.1002/nme.2360
51. Y. Y. Lu, T. Belytschko, and L. Gu, "A new implementation of the element free Galerkin method," *Computer Methods in Applied Mechanics and Engineering*, vol. 113, no. 3, pp. 397-414, 1994/03/01/ 1994, doi: https://doi.org/10.1016/0045-7825(94)90056-6.
52. S. Ren, P. Zhang, Y. Zhao, X. Tian, and S. A. Galindo-Torres, "A coupled metaball discrete element material point method for fluid–particle interactions with free surface flows and irregular shape particles," *Computer methods in applied mechanics and engineering*, vol. 417, p. 116440, 2023, doi: 10.1016/j.cma.2023.116440. https://doi.org/10.1016/j.cma.2023.116440
53. T. Strouboulis, I. Babuška, and K. Copps, "The design and analysis of the Generalized Finite Element Method," *Computer methods in applied mechanics and engineering*, vol. 181, no. 1, pp. 43-69, 2000, doi: 10.1016/S0045-7825(99)00072-9. https://doi.org/10.1016/S0045-7825(99)00072-9
54. M. Cremonesi, A. Franci, S. Idelsohn, and E. Oñate, "A State of the Art Review of the Particle Finite Element Method (PFEM)," *Archives of computational methods in engineering*, vol. 27, no. 5, pp. 1709-1735, 2020, doi: 10.1007/s11831-020-09468-4. https://doi.org/10.1007/s11831-020-09468-4
55. A. Larese, R. Rossi, E. Oñate, and S. R. Idelsohn, "Validation of the particle finite element method (PFEM) for simulation of free surface flows," *Engineering computations*, vol. 25, no. 4, pp. 385-425, 2008, doi: 10.1108/02644400810874976. https://doi.org/10.1108/02644400810874976
56. J. Xie, D. Nélias, H. Walter-Le Berre, K. Ogawa, and Y. Ichikawa, "Simulation of the Cold Spray Particle Deposition Process," *Journal of Tribology*, vol. 137, no. 4, 2015, doi: 10.1115/1.4030257. https://doi.org/10.1115/1.4030257
57. S. Rahmati and B. Jodoin, "Physically Based Finite Element Modeling Method to Predict Metallic Bonding in Cold Spray," *Journal of Thermal Spray Technology*, vol. 29, no. 4, pp. 611-629, 2020/04/01 2020, doi: 10.1007/s11666-020-01000-1. https://doi.org/10.1007/s11666-020-01000-1
58. A. A. Hemeda *et al.*, "Particle-based simulation of cold spray: Influence of oxide layer on impact process," *Additive manufacturing*, vol. 37, p. 101517, 2021, doi: 10.1016/j.addma.2020.101517. https://doi.org/10.1016/j.addma.2020.101517
59. A. Baluch, Y. Park, and C. G. Kim, "High velocity impact characterisation of Al alloys for oblique impacts," *Acta astronautica*, vol. 105, no. 1, pp. 128-135, 2014, doi: 10.1016/j.actaastro.2014.08.014. https://doi.org/10.1016/j.actaastro.2014.08.014
60. B. O'Toole *et al.*, "Modeling Plastic Deformation of Steel Plates in Hypervelocity Impact Experiments," *Procedia Engineering*, vol. 103, pp. 458-465, 2015/01/01/ 2015, doi: https://doi.org/10.1016/j.proeng.2015.04.060.

AUTHORS PROFILE

Mr. Mahendher Marri, a BEng (Hons) in mechanical engineering and has a diverse field background. As a Mechanical Engineering Specialist at Yamaha Motors in India, my understanding of engineering principles and their real-world applications. Later, I joined Heriot-Watt University as a Research and Teaching Assistant, where I honed my skills in academia and research. I then ventured into the industry as a Technical Support Specialist at CleanTech in Dubai, gaining practical experience in troubleshooting and problem-solving. My research interests encompass Heat Transfer, Finite Element Analysis, Tribology, 3D printing, and Artificial Neural Networks.

Dr. Rehan Ahmed, is a distinguished faculty member at Heriot-Watt University, specializing in advanced materials engineering. With a prolific research career, he has made significant contributions to the fields of thermal spray coatings, nanotechnology, and material degradation. Dr. Ahmed holds a PhD in Mechanical Engineering and has over 20 years of experience in academia and industry. He has published numerous papers in top-tier journals and is renowned for his expertise in surface engineering and advanced manufacturing. At Heriot-Watt, Dr. Ahmed is committed to pioneering research and mentoring the next generation of engineers.